Pulsed gas metal arc additive manufacturing of low-carbon steel: Microstructure observations and mechanical properties

Javad Mohammadi ¹, Iman Dashtgerd ², A. Reza Riahi ^{1,*}, Amir Mostafaei ^{2,*}

Abstract

Gas metal arc additive manufacturing (GMA-AM), also known as wire arc additive manufacturing (WAAM), uses an electric arc to melt a wire electrode and deposit objects layer by layer. This study focuses on creating single-pass wall structures using a low-carbon steel wire (ER70S-6) and examining the relationship between pulse frequency and weld geometry, microstructure, and mechanical properties. Microscopic observations showed a typical columnar microstructure with three distinct regions: acicular ferrite, bainite, and allotriomorphic ferrite in the first and last layers, while the mid-region exhibited homogenous polygonal ferrite grains with some pearlite at the grain boundaries. The tensile test results demonstrated a dependency of strength on the applied pulse frequency, with the highest strength (i.e., the ultimate tensile strength of 522 MPa and yield strength of 375 MPa with ductility of ~52%) achieved in parts processed at a frequency of 100 Hz. Vickers microhardness values revealed uniform hardness in the middle region, consistent with the microstructure observation. Analyzing thermal cycles, coupled with microstructure analysis and continuous cooling transition diagrams, provided insight into how phase and microstructure evolution occurred in low-carbon low-alloy steels processed through PGMA-AM.

Keywords: Wire arc additive manufacturing; Pulse current; ER70S-6 Steel; Microstructure; Mechanical properties.

¹ Department of Mechanical, Automotive and Materials Engineering, University of Windsor, Windsor, Ontario N9B 3P4, Canada

² Department of Mechanical, Materials, and Aerospace Engineering, Illinois Institute of Technology, Chicago, IL 60616, USA

^{*} Corresponding authors: ariahi@uwindsor.ca (A.R. Riahi), mostafaei@iit.edu (A. Mostafaei)

1. Introduction

Additive manufacturing, which is commonly referred to as 3D printing, has brought about a significant transformation in the way we design, prototype, and manufacture products. This revolutionary technology has gained immense popularity in recent years, especially in the field of metal 3D printing. Metal 3D printing has captured much attention due to its unique ability to produce intricate geometries, minimize waste, and enhance material properties [1-3]. Wire arc additive manufacturing (WAAM) is an emerging technology that has gained significant attention from researchers and industry professionals alike due to its ability to produce large-scale, complex components using a wire as the feedstock material. The technology has been used to fabricate components from a range of materials, including metals, polymers, and composites, with applications in aerospace, automotive, and biomedical industries [4]. In WAAM, a wire electrode is melted using an electric arc to deposit material onto a substrate or previous layer, which then solidifies to create the desired shape. This process can be used to create large, complex metal parts with high precision and strength [5, 6].

Like other fusion-based AM processes, the WAAM process involves the progressive melting and solidification of the material being deposited, which can lead to the development of various solidification defects. These defects may include discontinuities, such as hot cracks, pores, inclusion, and lack of fusions, as well as microstructural imperfections and inhomogeneity, such as grain coarsening and the formation of brittle phases within the heat-affected zone (HAZ) [7-10]. Compared to powder-based additive manufacturing, WAAM is more efficient at creating low to medium-complexity and large-scale preform components because it can achieve an incredibly high deposition rate through two different methods: (1) using wires as the feed material into the weld puddle or (2) using an electric arc or plasma in gas tungsten arc (GTA) or gas metal arc (GMA) as the heat source [7-9]. The deposition of the metal droplet in WAAM is complex due to the role of arc force, which is formed of four elements: the electromagnetic force, plasma flow force, arc pressure, and particle charged by a force field [11]. Consequently, many researchers have investigated gas metal arc additive manufacturing (GMA-AM) processes to determine the optimal operational parameters for materials and to achieve higher deposition rates [12-16]. These factors significantly affect the properties of the end products, including their quality and desirability.

Low-carbon, low-alloy (LCLA) steels are widely used in various engineering applications due to their excellent strength, toughness, and corrosion resistance. WAAM has been used to manufacture low-alloy steel components with different microstructures and mechanical properties [11, 17]. In the case of WAAM-produced LCLA steels, the relationship between these parameters is complex and interdependent. Previous research [12-16] has shown that the microstructure of WAAM-produced LCLA steels is highly dependent on the process parameters. The process parameters, including the wire feed rate, arc voltage, and travel speed, determine the temperature and cooling rate during deposition, which in turn affect the microstructure of the material. The microstructure, including grain size, phase composition, and morphology, has a significant impact on the mechanical properties of the material, such as yield strength, tensile strength, and ductility [11, 18].

Zhang et al. [19] showed that increasing the travel speed resulted in finer and more uniform grains due to the increased cooling rate. Similarly, Wang et al. [20] studied the role of wire feed rate on the microstructure of WAAM-produced high-strength low-alloy steel and reported that increasing the wire feed rate resulted in a finer microstructure and higher hardness. Zhang et al. [16] considered the influence of deposition parameters on the microstructure of wire arc additively manufactured ER 70S-6 alloy steel. The study found that increasing the wire feed speed and the welding voltage led to an increase in the dilution rate, resulting in a decrease in the microhardness of the deposited material. Furthermore, increasing the deposition rate resulted in a coarser microstructure with larger grain sizes. Rafizadeh et al. [21] conducted a study on a low-carbon, low-alloy steel component manufactured using WAAM to characterize the microstructure and mechanical properties. The microstructure of the component contained ferritic grains with a small amount of pearlite at their grain boundaries in the deposition direction. However, the center of the melt pool displayed a combination of acicular ferrite and bainite with polygonal ferrite. They characterized that tensile strength, elongation, and Charpy impact were higher in the horizontal direction of the component than in the vertical direction. This difference was attributed to the presence of a uniform ferritic microstructure.

Haden et al. [22] observed an absence of noticeable anisotropy in mechanical properties, including yield and tensile strength, within LCLA steel (ER70S-6) produced using WAAM. However, in their study, the reported mechanical properties were not conclusively linked to the microstructure of the additively manufactured wall. In a recent study by van Tao et al. [17], GMAW welding system was used to additively manufacture the LCLA steel ER70S-6 along the two depositing directions followed by a detailed

microstructure and mechanical properties investigation and thin walls display diverse microstructures: upper - lamellar, middle - granular, bottom - mixed grains. Liu et al. [23] investigated the effect of heat treatment on the microstructure of WAAM-processed ER 70S-6 alloy steel. The study indicated that heat treatment resulted in the formation of a more refined microstructure with a higher fraction of precipitates, which improved the mechanical properties of the deposited material. Wu et al. [24] examined the impact of process parameters on the tensile properties of WAAM-produced highstrength low-alloy steel and showed that increasing the wire feed rate and decreasing the travel speed resulted in higher tensile strength and yield strength. However, the ductility of the material decreased with increasing wire feed rate due to the coarsening of the microstructure. Xu et al. [25] found that increasing the wire feed rate and decreasing the welding speed led to an increase in the hardness of the deposited material. Xu et al. [25] showed that the tensile strength of the deposited ER 70S-6 alloy steel was affected by the microstructure and deposition parameters, with higher tensile strengths observed for materials with a finer microstructure and lower dilution rates. Pulsed gas metal are additive manufacturing (PGMA-AM) is a current-controlled short-circuit metal transfer mode that is part of the gas metal arc welding (GMAW) process. What sets PGMA-AM apart from other transfer modes is its ability to reduce energy consumption while also providing better control over the fusion zone on a droplet-by-droplet basis. This control allows to produce smoother bead profiles and improved bead geometries, making it an attractive option for minimizing the softening of the heat-affected zone (HAZ). Compared to conventional spray or cold metal transfer, PGMA-AM has a significantly lower heat input, with the potential for energy savings of up to 80% [26-28]. By enabling a fast-cooling process, PGMA-AM has the potential to dramatically enhance the strength of high-strength low-alloy steels. However, the capabilities of this transfer mode for the WAAM of metallic components have not been reported in the existing literature.

The PGMA-AM is a promising transfer mode for the WAAM of metallic components due to its energy efficiency, better control over the fusion zone, and potential for improved strength. Further research is needed to fully explore the capabilities and limitations of this transfer mode for WAAM applications. While a considerable amount of research has been conducted on the use of pulsed WAAM for fabricating Ti-6Al-4V alloys [22, 29, 30], there has been relatively less investigation into its application for steel production. The proposed steel is one of the most widely used materials in modern industry including structural steels, auto bodies, pipes, fittings, castings,

and forgings [31-33]. Therefore, this study aims to address this gap by using WAAM to fabricate low-carbon low-alloy steel (i.e., ER70S-6), with a focus on the utilization of pulse voltage waveform control technology. This study presents a detailed analysis of the microstructure and mechanical properties of WAAM thin wall parts and examines the impact of the manufacturing process on the anisotropy of mechanical properties and microstructure characterization. The study employed both tensile testing and fractography techniques, investigating mechanical properties in vertical and horizontal directions.

2. Experimental Procedure

2.1. Pulsed gas metal arc additive manufacturing (PGMA-AM) process

In this study, a commercially available filler metal of ER70S-6 wire with a diameter of 0.8 mm and chemical composition given in Table 1 (according to AWS designation) was used to deposit 40 consecutive monodirectional layers with approximate dimensions of $150 \times 65 \times 5$ mm³ wall on a low-carbon steel 1018 substrate using the Pulsed Gas Metal Arc Additive Manufacturing (PGMA-AM) process. Before the deposition process, the substrate surface was cleaned with a stainless-steel brush and degreased with acetone. The Everlast power supply (model MTS 251 SI) was used to control the travel speed and path of the torch by using a three-axis CNC machine.

Table 1. Chemical compositions (wt.%) of filler metal and substrate.

Element	C	Si	Mn	P	S	Cr	Mo	V	Cu	Fe
ER 70S-6	0.15	0.80	1.40	0.15	0.03	0.15	0.005	0.05	0.02	Balance
1018 CS	0.17	0.22	0.85	0.02	0.03	-	-	-	-	Balance

The power source used in this study is different from other power supplies used with pulse metal inert gas (MIG) systems as it employs pulsing voltage instead of pulsing current. Pulsing voltage allows heat input to be controlled and minimized by creating an average voltage value that preserves the optimum characteristics of lower and higher voltage values. Pure Ar gas (99.999%) was used as a shielding gas with a flow rate of 20 L/min. Synergic and pulse programs in pulse mode were used, and Table 2 summarizes four processing conditions. Both the base voltage and the MIG inductance were set at 50%. The pulse time directly influences the heat input. By adjusting the pulse time, the value of applied heat is controlled to the welding area during each pulse. Shortening the pulse time reduces the heat input for that specific duration, which can be useful for

preventing excessive heating and controlling the size and penetration of the weld bead. Figure 1 shows the schematic of the PGMA-AM process.

Table 2. Used processing parameter during PGMA-AM process. Adjustment of pulse time decrease the rate of pulse time in the WAAM process.

No.	Voltage (V)	Current (A)	Frequency (Hz)	Pulse Time On (%)		
1	19±1	80±10	50	1 st -10 th :75		
2			100	11 th -30 th : 50 31 st -40 th : 25		
3			150			
4			200	31 -40**: 23		

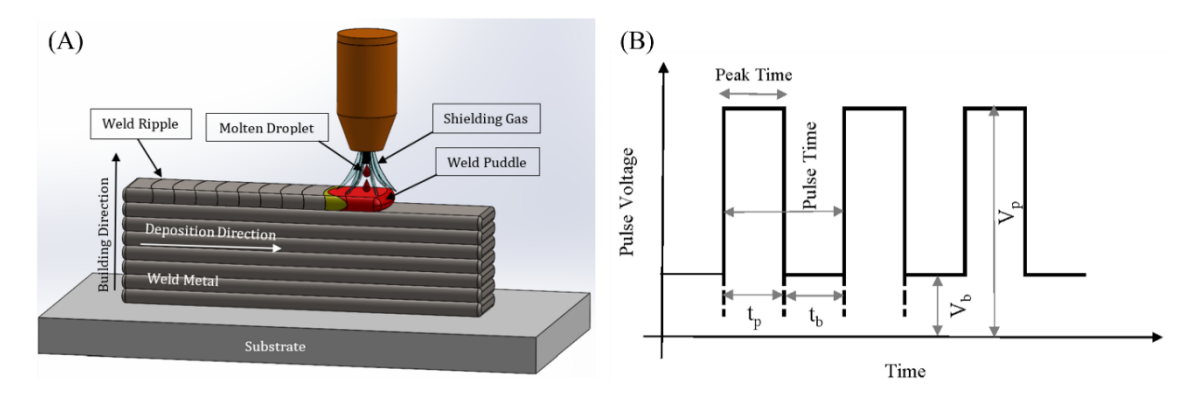


Figure 1. (A) Schematic of pulsed gas metal arc additive manufacturing system and (B) diagram of a standard pulse voltage-time waveform applied in the PGMA-AM process (V_p = peak current; V_b = background current; t_p = pulse on time; t_b = pulse off time).

The ER 70S-6 wire was deposited using a layer-by-layer deposition method to a 40-layer height with a bead width of ~ 5 mm. The travel speed was 7.0 mm/s, and the wire feed rate was set at 68 mm/s. The time interval between the deposited layers was set at 90 s, which was enough to reduce the temperature below the phase transition temperature of the deposited material.

2.2. Characterizations

Figure 2(A) presents an exemplary view of the deposited materials on the substrate. For microscopy observations, samples were sectioned parallel to the build direction of each deposited wall. Subsequently, specimens were mounted with epoxy resin, ground with sandpapers up to 2400 grit, and polished using a 1 µm diamond paste solution. The sample surfaces were sonicated in acetone for 5 minutes to avoid the presence of impurities. Etching was performed using 2% Nital solution. Microstructural observations were conducted using a Keyence laser scanning microscope

(VK-X100) and scanning electron microscopy (SEM, model FEI Quanta 200 Environmental SEM) equipped with an EDAX Octane Plus SDD Detector. X-ray diffraction pattern (XRD) was carried out on selected samples using an x-ray diffractometer (model Thermo ARL) with Cu-K α radiation (λ = 1.5406 Å, 35 kV and 30 mA), a 2 θ ranging between 30 and 100°, a scan speed of 1 s/step, and scan step of 0.02 ° at an ambient temperature. Vickers microhardness measurements were taken using a Buhler Vickers microhardness tester (MICROMET II) at a load of 200 g and a dwell time of 10 s. Vickers microhardness measurements were carried out at the centerline along the building direction. To prepare the flat tensile specimens, the deposited walls were cut in both horizontal and vertical directions, as shown schematically in Figure 2(B), with dimensions presented in Figure 2(C). Room temperature tensile tests were then carried out using a universal testing machine (MTS 50KN) with crosshead speed of 2 mm/min. The selected samples for the Charpy impact tests were made according to ASTM E23–18. The absorbed energy by each sample during fracture was obtained at six different temperatures, i.e., -150, - 100, - 50, 0, and 23 °C (room temperature), using an automatic impact testing apparatus (a JBS-300 machine) with the maximum capacity of 300 J. Finally, fracture surfaces of tensile test samples were studied using SEM.

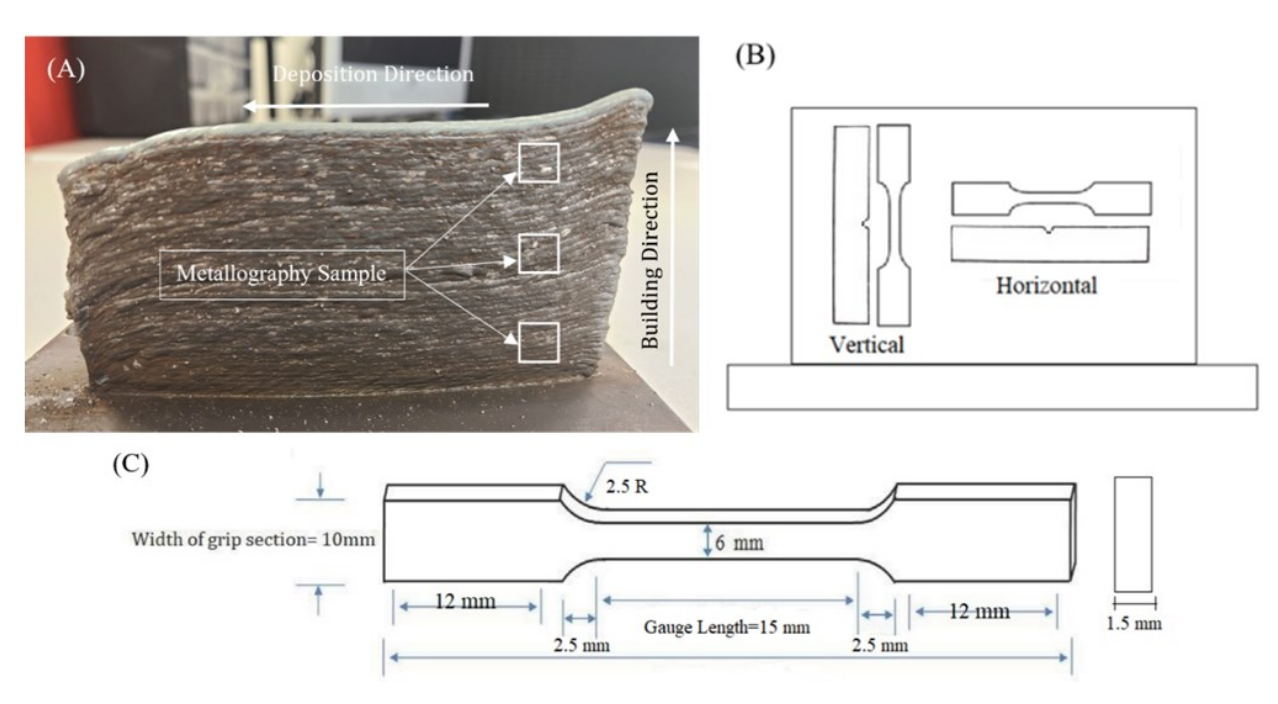


Figure 2. (A) As fabricated thin-wall deposited materials, indicating locations of the selected sections for microstructure observations, (B) location and direction of tensile and impact samples, and (C) the dimension of prepared tensile specimens.

3. Results and discussion

3.1. Microstructure of deposited layers

In Figure 3(A), the cross-sectional optical micrographs of ER70S-6 steel samples deposited at various frequencies and multi-pass layouts from the substrate to the top are displayed. The layers deposited on the substrate up to the middle region exhibit a concave and parallel band, whereas the top layer has a convex band. The heat-affected zone is defined as the concave area that extends to the surface with a higher inter-pass temperature. Moreover, an increase in frequency from 50 Hz to 200 Hz resulted in an increase in the width of the deposited materials. To analyze pore formation, longitudinal cross-sections were conducted through the center of the walls. Porosity within these cross-sections was assessed (using ImageJ software) by manually quantifying the quantity and dimensions of pores. The relative number of pores represents the average count of pores within a single layer, determined manually within the cross-sectional analysis.

Porosity analysis indicated that the part deposited by 100 Hz had 0.11% porosity which was the lowest pore fraction amongst other deposited samples (see Figure 3(A)). Five different areas are selected on each specimen for microstructure observations, and optical micrographs are shown in Figure 3(B). It is observed that there are three main regions: (1) the last layer, in which the grain structure consists of coarse columnar grains, (2) the first layer, in which the grain structure is composed of fine columnar grains, and (3) the middle area, where the grain structure is composed of ultrafine, equiaxed grains.

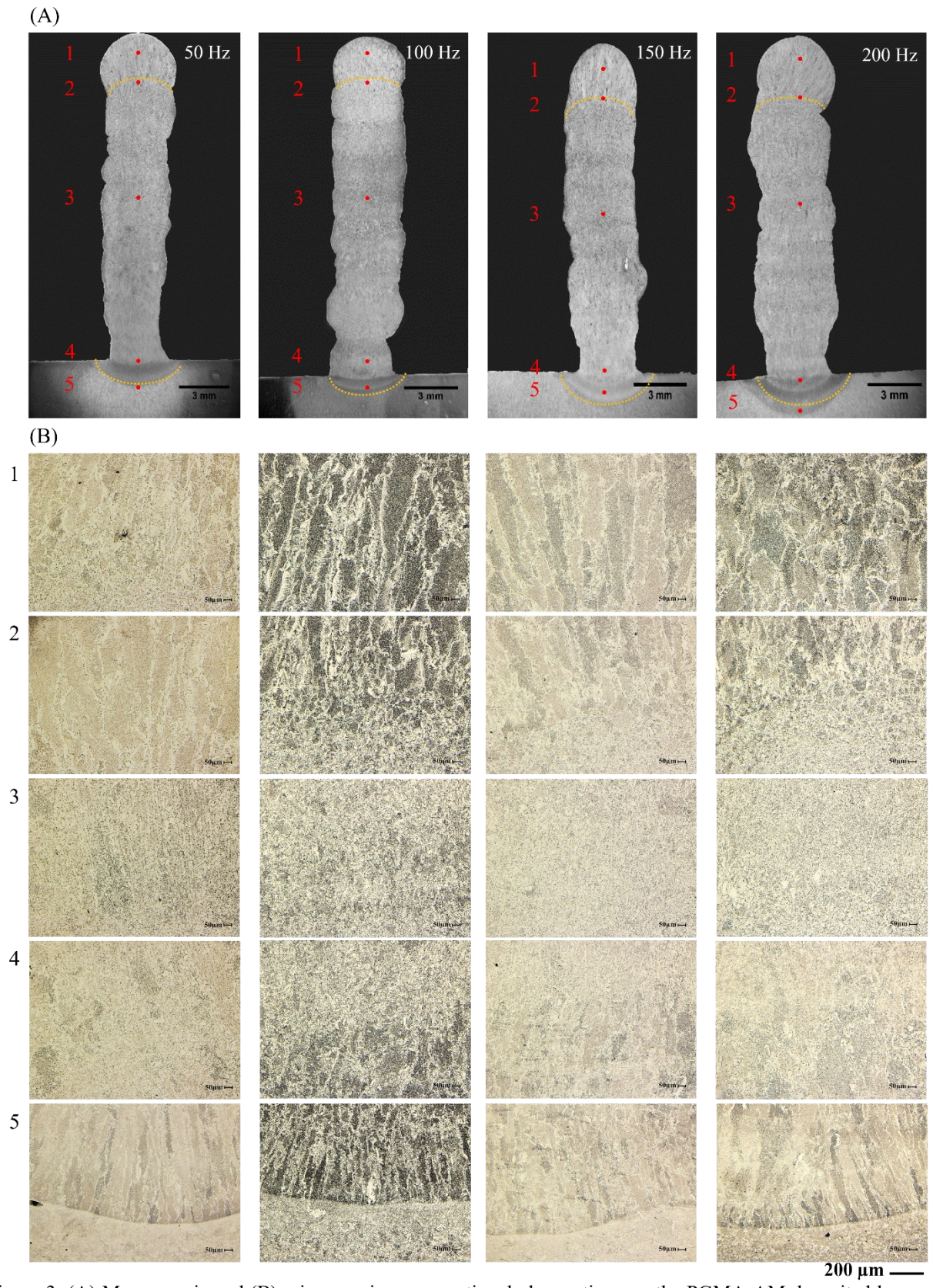


Figure 3. (A) Macroscopic and (B) microscopic cross-sectional observations on the PGMA-AM deposited layers at different frequencies. Five different regions were presented on each sample to compare grain structures.

To further analyze the microstructure, two deposited walls using 100 Hz and 200 Hz were selected, and the results are presented in Figure 4. Different locations relative to their solidified bead height were selected to observe microstructure and phase formation. When the first layer was deposited on the substrate (lower region), partial melting of the base plate occurred, and solidification took place upon cooling. It was evident that the nucleation and growth of grains at the interface of the fusion zone and substrate followed fine grain structure on the wrought alloy with proeutectoid ferrite (F) and pearlite (P), then directional solidification resulted in typical columnar grain growth. In the fusion zone of the lower region, the columnar grains are composed of allotriomorphic ferrite (ALF), acicular ferrite (AF), and bainite (B). A high fraction of ALP phase was characterized at the grain boundaries in the lower region in agreement with [22, 34, 35]. Also, the dark areas within the grains represent AF and B, whereas the white regions represent ALP which was transformed across the prior austenite grain boundaries. As indicated in Figure 3(B), only a small area on the very bottom parts of the deposited material showed elongated columnar grain along the heat dissipation direction.

As the new layers were deposited, thermal cycles caused reheating of the previous layers, thus, the inter-pass cooling rate slightly decreased, and the dominant microstructure in the middle part of the deposited wall (2<X<Y-2 where X is the height in mm located in the middle part of the deposited wall and Y is the total height) showed polygonal ferrite (PF) and fine grain ferrite (FGF) with a slight volume fraction of pearlite (P) on the grain boundaries. The upper region of the deposited wall (last layer) showed an elongated upper layer that consists of a mixture of the typical AF, B, and ALF. These constituents are similar to the first few layers of the deposited wall on the bottom region.

In the last layer, the homogeneous region of PG from the middle layer transforms to a mixed microstructure due to the higher thermal gradient and supercooling rate. The height of the last layer was almost twice as high as those of the previously deposited layers because of the remelting and mixing of the previously deposited layer into the subsequent layers [36]. It was also seen that elongated ferrite grains formed epitaxially from the top region (n-1 layer) of the fusion zone, which is normally parallel to the build direction. The transition zone was distinguished from the coarse-grain structure above it by its fine-grain structure. The peak temperature in the transition zone caused a complete transformation to austenite, and then a phase transition from *austenite* \rightarrow *bainite* + *ferrite* took place due to the rapid cooling rate [3]. Coarse grains in this area include

ALF, and minor quantities of AF and B (all phases were labelled in Figure 4). Liberini et al. [37] identified different microstructures of the various zones achieved by continuous deposition of weld beads using an ER70S-6 steel wire by GMA-AM process. They also characterized the microstructural inhomogeneity in all samples through the deposited wall, finding a ferritic structure with three key elements: (1) a lamellar structure that is typically bainitic at the upper zone of the wall, (2) thin strips of pearlite at the lower zone, and (3) equiaxed grains of ferrite in the middle zone. They concluded that the difference in the various microstructures from the bottom to top was due to the different thermal cycles experienced with the different deposition sequences and paths.

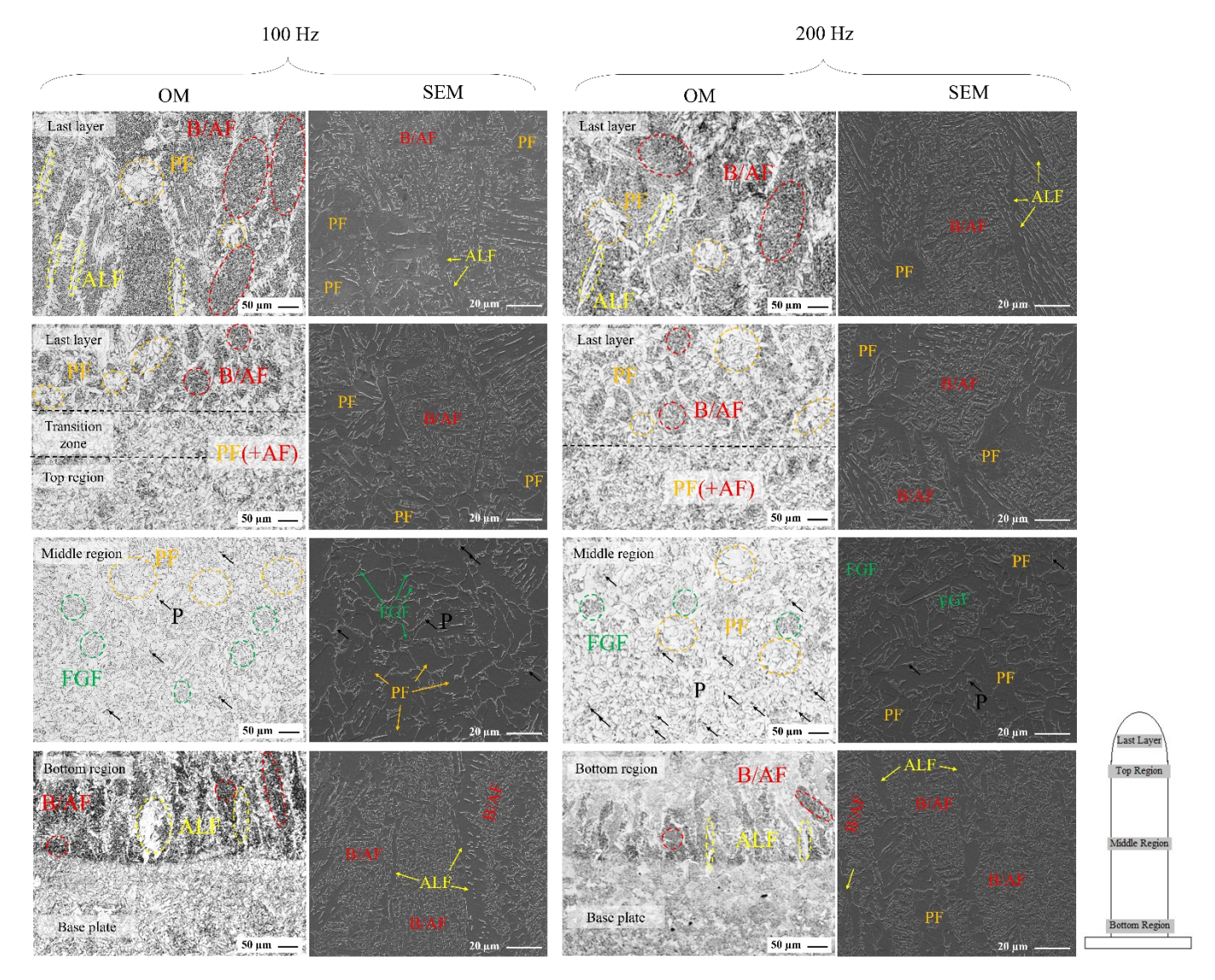


Figure 4. Microscopy observations using optical and scanning electron microscopy on two selected specimens, i.e., PGMA-AM processed samples using 100 Hz and 200 Hz.

Figure 5 shows the measured grain size in three different area of the deposited materials. The last layer labelled as "1" belongs to the top 2 mm of the deposited alloy. The average grain size of 1.5-4.0 μm was measured in this region. The areas labelled as "2 to 9" belong to the middle region (2<X<Y-2 where X is the height in mm located in the middle part of the deposited wall and Y is the total height) in which the average grain size of 10-15 μm was measured. The area labelled as "10" belongs to the first deposited layer on the substrate, and the measured average grain size was 1.5-4.0 μm. Fine grain ferrite (FGF) and polygonal ferrite (PF) with a small fraction of pearlite (P) characterized as black regions on multiple grain points were seen in the middle region of collected micrographs in Figure 4. There was a more homogenous microstructure in the middle section compared to the lower or upper region of the thin wall deposited at different pulse frequencies, where equiaxed grains were observed with thin pearlite. The high thermal shock and lower inter-pass cooling rate occurring at the upper section induced a rather consistent grain structure.

The grain size is significantly influenced by the pulse frequency, which impacts the grain refinement process in two ways: by stirring the motion in the weld puddle and increasing cooling rates. Firstly, pulse voltage affects the motion of the weld puddle by stirring it, which improves the refining process. Higher frequency builds plasma momentum rapidly and generates an electromagnetic force [11, 30]. The plasma momentum causes are pressures and shearing forces on the molten puddle's surface. These electromagnetic forces drive the molten puddle fluid outward into the weld and then down to the weld axis [38]. This action generates enough oscillations in the molten puddle to create more heterogeneous nucleation sites and refine the grain size. The increasing pulse frequency increases molten puddle oscillations in line with the theories of welding ripples, and the impact of grain refining grows [39].

Secondly, pulse voltage increases the cooling rate of the molten puddle, which accelerates the refining of the grains. The peak voltage produces heat to melt the wire, whereas the lower values of the base voltage control the arc. The heat input decreases unexpectedly during the application of the base voltage. Consequently, the higher cooling rates in the molten puddle increase heterogeneous nucleation, which modifies the grains [40, 41]. As the pulse frequency increases, the heat input stays stable. The arc pressure also rises with increasing pulse frequency, causing the arc to initially possess a wide and conical form, gradually becoming narrower and finally tending to a stable, roughly cylindrical shape [29].

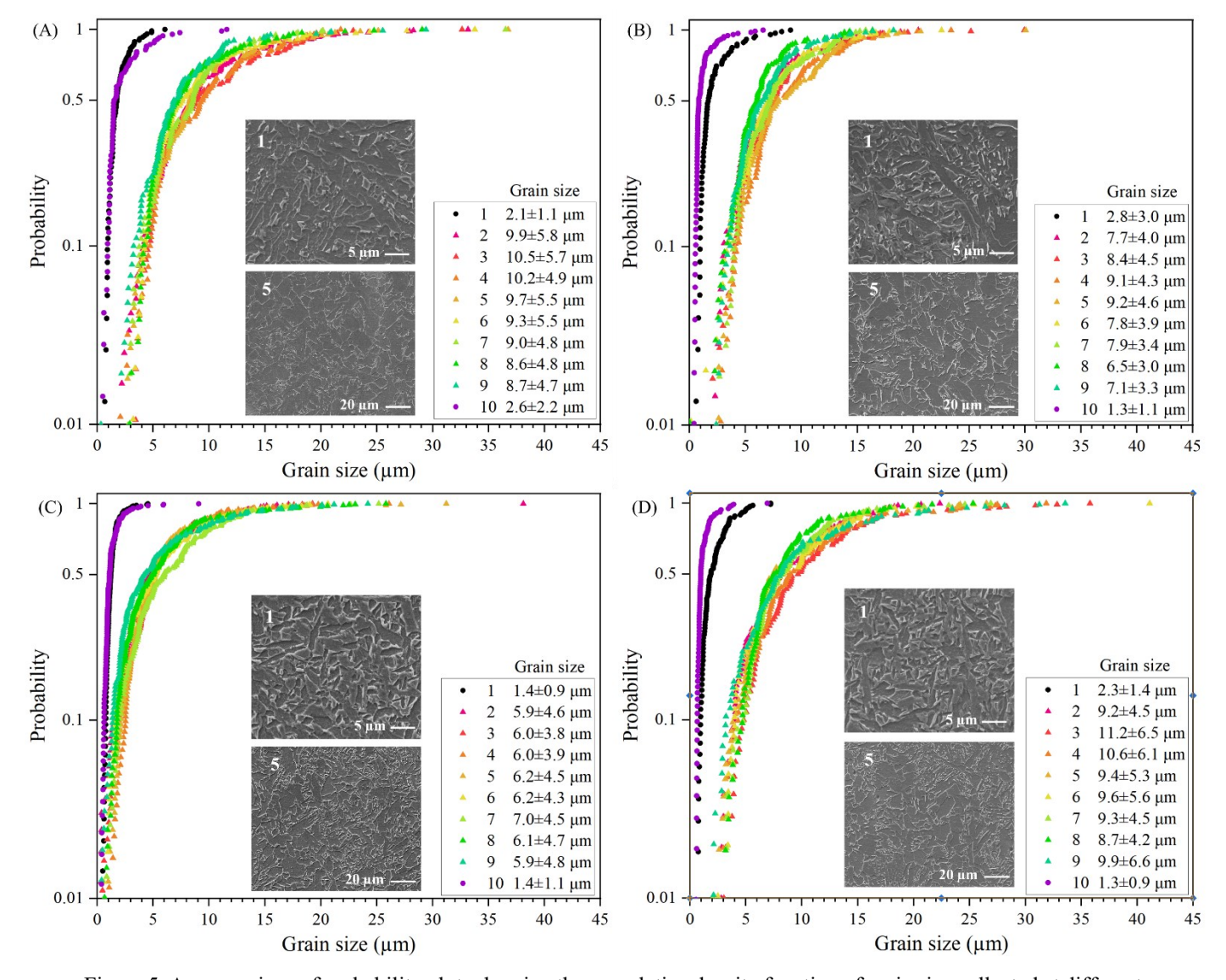


Figure 5. A comparison of probability plots showing the cumulative density function of grain size collected at different areas of the deposited layers using pulse frequencies of (A) 50 Hz, (B) 100 Hz, (C) 150 Hz, and (D) 200 Hz. Area 1 and 10 were in the last and first layers, respectively, and the rest of the measurements were in the middle area. The inserted SEM micrographs demonstrated the morphology of grains in the last layer and middle area.

When the pulse frequency is increased in PGMA-AM, the on-time of the arc becomes shorter, and the off-time becomes longer. The welding arc is active for a shorter duration (shorter on time) before it cycles off. Consequently, the off time, when the arc is not active, becomes longer. Consequently, the off time, when the arc is not active, becomes longer. If the pulse duty ratio is constant while increasing the pulse frequency, the same proportion of on-time to off-time within each pulse cycle is maintained. However, because the overall cycle time is shorter, the heat input per unit of time (rate of heat input) decreases. This can be advantageous to control the amount of

heat delivered to the workpiece more precisely over time. This results in a reduction in the total energy input and a decrease in the heat input per unit time. Consequently, the temperature of the molten pool decreases, and the solidification rate increases. A higher solidification rate can lead to a finer microstructure, reduced porosity, and improved mechanical properties, such as higher strength and hardness. Therefore, when the pulse frequency increased from 50 Hz to 150 Hz, a reduction in ferritic grains was observed. Conversely, when the pulse frequency is decreased, the on-time of the arc becomes longer, and the off-time becomes shorter. This results in an increase in the total energy input and an increase in the heat input per unit time. Therefore, the temperature of the molten pool increases, and the solidification rate decreases. A lower solidification rate can lead to a coarser microstructure, increased porosity, and lower mechanical properties. However, it is important to note that the relationship between pulse frequency and heat input in WAAM is not always linear. At very high pulse frequencies, the heat input may start to increase again due to the difficulty in maintaining stable arc behavior. This was the case when a pulse frequency of 200 Hz was used and resulted in the coarsening of ferritic grains. The optimum pulse frequency, which is 100-150 Hz, produces weld layouts containing finer and uniformly equiaxed grains.

3.2. Understanding process-microstructure relationship in PGMA-AM of LCLA steels

3.2.1. Thermal analysis

Solid-state transformations occurring during multiple cooling and heating cycles are a major concern in WAAM. The formation of the columnar grain zone (CGZ) during solidification is accompanied by a high concentration of ferrite grain boundary. As a result, a comprehensive analysis of specific thermal events and their effects on microstructure evolution due to solid-state transformations is essential to gain a better understanding of the homogenized zone. Figure 6 illustrates the oscillation of voltage-current-temperature against time during PGMA-AM processing of ER70S-6 steel. The thermal history was recorded using K-type thermocouples (see Figure 6(C)), which were installed at a 2.5 mm distance from the melt pool to avoid possible melting of the thermocouples. Despite the placement of the thermocouple in the substrate, which suggests lower temperatures compared to those present in the deposited layer, it is still possible to discern the overall trend in thermal cycles for each deposition mode used to create the walls. Specifically, the cooling rate was slower when frequencies of 50 Hz to 150 Hz were applied, leading to prolonged exposure of the previously deposited layers to thermal cycling, while it was significantly faster at the frequency of 200 Hz, resulting in a cooling rate at much higher rates.

Considering the microstructural observation (refer to Figure 4) and resulting mechanical properties (refer to Figure 10), the alloy deposited at a frequency of 100 Hz displayed the most favorable microstructure-property relationship. As a result, our focus for the study of microstructure and further exploration of thermal cycling and in-situ heat treatment will be centered around this particular sample.

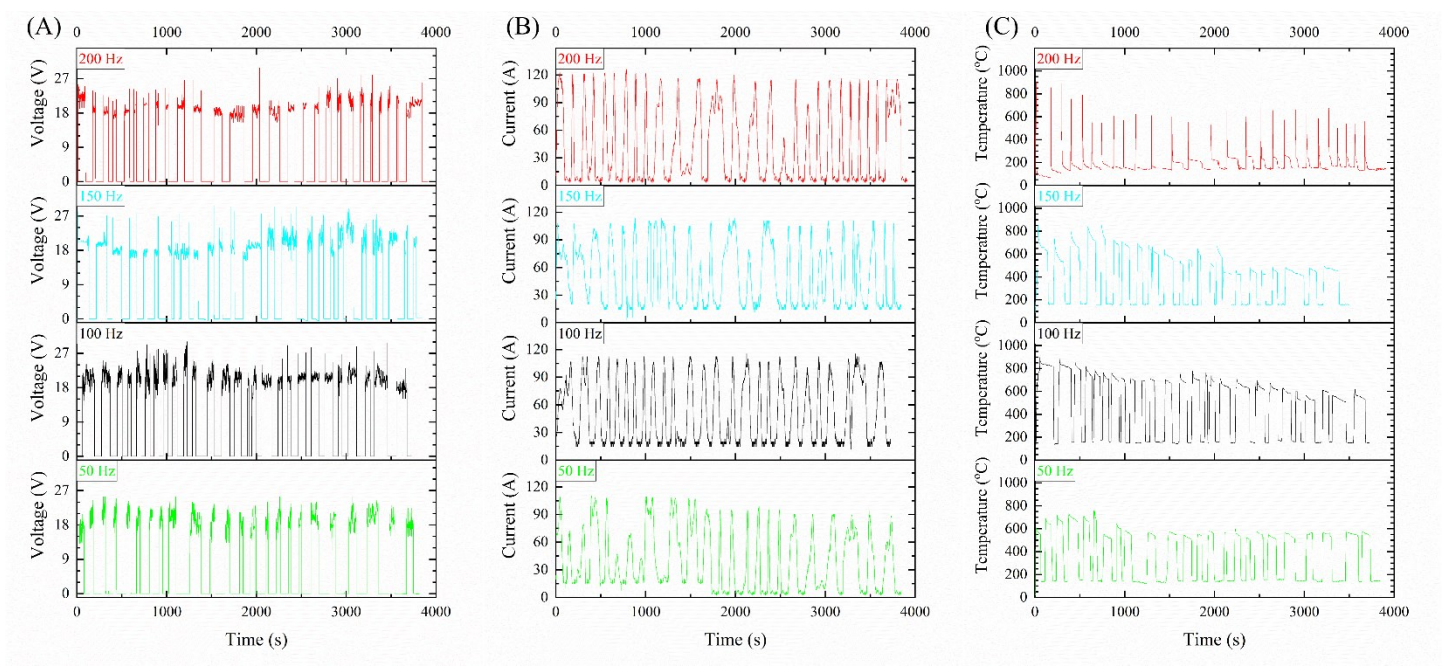


Figure 6. (A) Voltage, (B) current, and (C) thermal history of the PGMA-AM processed ER70S-6 steel.

As illustrated in Figure 6(C), it can be observed that during layer 2^{nd} and layer 3^{rd} in 100 Hz mode, the peak temperature exceeded the solidus temperature. Variation of ferrite and austenite volume fractions against temperature was calculated using JMatPro, suggesting γ -transus temperature of AC₃=863 °C and pearlite transus temperature AC₁=725 °C (see Figure 8 (D)). Furthermore, the Continuous Cooling Transformation (CCT) diagram was generated by exporting data from the JMatPro software for the specified composition, shown in Figure 8 (E). By layer 3^{rd} , the temperature had surpassed the γ -transus temperature (AC₃, 858 °C, which was calculated based on the alloy composition) [42, 43], resulting in a coarse-grained area as shown in the bottom portion of Figure 4. The peak temperature was measured to be 898°C, slightly higher than the γ -transus. Consequently, the microstructure at a depth of 4.5 mm (equivalent to three layers from the bottom) was normalized. This implies that the austenitizing temperature can be extended to a distance equivalent to three consecutive layers by just one melt layer, as indicated in Figure 6(C). In layer 4^{th} to layer 7^{th} , it was observed that the second measured peak temperature (780 °C)

exceeded the temperature (AC₁, 733 °C, which was calculated based on the alloy composition) [43], at which the volume fraction of the γ-phase increases significantly (AC₁, 733 °C). This suggests that following full γ-normalization, the microstructures underwent heat treatment like inter-critical annealing, corresponding to the inter-critical HAZ. However, during layer 8th, the measured peak temperature (716 °C) did not reach AC₁, which is equivalent to tempering and corresponds to the subcritical HAZ. As the heat source moved upwards, the temperature gradient gradually decreased, resulting in the peak temperature of the subsequent thermal cycle remaining relatively stable for a longer period. Following the normalization and inter-critical annealing steps due to thermal cycling, the deposited material underwent tempering, which was carried out continuously throughout the entire process.

3.2.2. Phase analysis using XRD

The XRD analysis of the deposited walls created through WAAM on ER70S-6 low alloy steel was carried out to identify the phases present in samples collected from various heights along the building direction. The results are depicted in Figure 7. As clearly indicated, the as-deposited walls are primarily composed of the ferrite phase, with α -Iron peaks observed at 2θ angles of approximately 44.6° , 64.8° , 82.2° , and 99.0° . Additionally, the XRD analysis revealed the presence of a small amount of second phase. This could be related to the retained austenite.

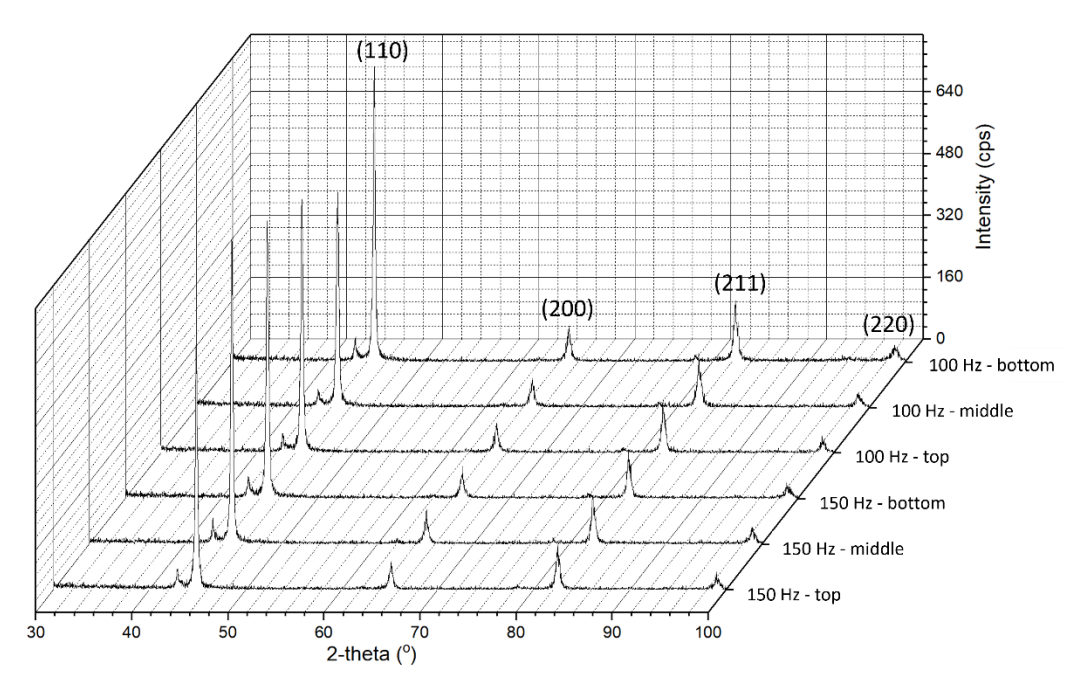


Figure 7. XRD analysis of the WAAM on ER70S-6 low alloy steel at the cross-sections parallel to the build direction. Two frequencies of 100 and 150 Hz were selected for analysis.

3.2.3. Intrinsic heat treatment (IHT)

In the initial thermal cycle, the temperature above AC₃ remained constant for a short time, 2-3 s, while remaining in the dual-phase zone for about 14-21 s. It is anticipated that the actual peak temperatures of the first three layers were significantly higher than the γ -transus, therefore, underwent a faster heating rate for a more extended period. In LCLA steels, such as ER70S6, the rapid cooling rate during WAAM and multiple thermal cycles result in rapid austenitizing of the deposited materials, which positively affects the microstructure evolution to eliminate dynamic strain aging [23, 44, 45]. Similar behavior was also reported in submerged arc additive manufacturing of LCLA steel [45]. Hence, by utilizing heat dissipation in a direction opposite to the buildup and employing a thinner single bead, the deposited material benefits from enhanced heat accumulation. This accumulation enables the material to surpass the γ -transus temperature while also penetrating previously formed layers (up to three layers), leading to a prolonged residence time within the system.

The process of PGMA-AM can lead to grain refinement and homogeneity by allowing for rapid austenitization of each layer beneath the fusion line at least twice with a relatively thin single bead [21, 46-48]. This is possible because a distance equivalent to two consecutive layers beneath the fusion line can be rapidly austenitized in a single melt layer. Once the austenitization and subsequent cooling process are finished, the layer undergoes inter-critical annealing, resulting in partial grain refinement [49, 50]. In multi-pass PGMA-AM, a thin fine-grained area, which is γ -normalized, can be observed between two adjacent layers (see Figure 4, second row, 100 Hz). In contrast, in other WAAM methods, such as metal inert gas and tungsten inert gas WAAM, inadequate matching strategies between layer thickness, heat input, and heat dissipation hinder the heat from penetrating the previous layer fully, making it challenging to obtain a microstructure that is fully tempered for the entire layer's duration [49-52].

3.2.4. Mechanism of microstructure evolution

The initial microstructure of the LCLA steel manufactured by PGMA-AM is typically composed of a mixture of ferrite and pearlite. Section 3.2.2 discussed the temperature evolution leading to the remelting of three prior layers, inducing a continuous change in the microstructure below the fusion line during PGMA-AM. Panchenko et al. [53] and Hackenhaar et al. [54] explain that the temperature gradient decreases as the heat source moves incrementally upwards. The

previously deposited material is affected by one melt experience resulting in subcritical heat-affected zones, CGZ, FGF, and PF. The evolution of microstructure in the CGZ and HAZ regions was schematically displayed in Figure 8(A) and compared with an actual deposited part from layers 27th to 30th, shown in Figure 8(B). As discussed in 3.1, equiaxed, fine ferrite was the dominant microstructure in this region.

When the 30th layer of molten metal is applied over the 29th layer with a bead height of approximately 2 mm, the local columnar grain zone and coarse-grained heat-affected zone (CG-HAZ) of the previously deposited layer will be subjected again to the temperature at which the previous microstructure underwent complete γ-normalization but had not yet undergone coarsening. This temperature lies within the range of normalizing, AC₃ < T < 1050 °C and is indicated in Figure 8(A), (the solid black line). This process promotes the formation of uniform FGF and ensures its dominance in the area influenced by the temperature in the range of AC₃-1050 °C. The temperature measurement plot reveals that the first peak temperature reached 900 °C, which falls within the temperature range of AC₃-1050 °C, as indicated by a black arrow in Figure 8(A), see " a_1 ". As a result, a significant portion of the fine-grained ferrite (FGF) in the 29th layer undergoes inter-critical annealing within the temperature range of AC₁-AC₃. This process leads to the decomposition of pearlite colonies into extremely fine FGF and pearlite in the 30th layer as they cool down from the slightly expanded austenite, as shown by the red line in Figure 8(B). The size of ferrite grains in the 29th layer remains restricted to their initial small size, averaging around 4 µm, due to the expansion of prior ferrite colonies during inter-critical annealing [55, 56].

The short annealing time, less than a few seconds, as indicated in Figure 6(C), also plays a role in restricting the size of ferrite grains. As a result, the inter-critically reheated FG heat affected zone (FG-HAZ) in this region will mainly consist of ferrite with a relatively uniform size, defined as partially refined ferrite ~1-4 µm. However, no visible changes in the previously deposited materials ferrite occurred when it was reheated by layer 30th to below AC₁ represented by the blue line in Figure 8(C). The continuous variation in temperature and bead height during the welding process leads to a gradual change in the microstructure of each sub-HAZ, which is affected by the subsequent layers. The measured temperature provides valuable information for predicting the final microstructure of each sub-HAZ in the deposited layers, which will be affected by the

subsequent layers with different temperatures and bead heights. The microstructure in the subcritically reheated FG-HAZ in the inter-critically reheated FG-HAZ contributes to the overall mechanical properties of the welded joint. The formation of a fine softened matrix leads to a microstructure that contains less and homogeneously distributed strain, resulting in improved mechanical properties. The smaller FGF size implies that there are more grains per unit area, leading to a more even distribution of the austenite to ferrite transformation strain across the grains, which also contributes to the improved mechanical properties of the material.

The HAZ bands are formed when the previously welded layer is reheated by subsequent layers to a temperature above AC₁ but cannot be austenitized. The HAZ bands can be observed in almost all AM components, and the components examined in this study are no exception. Similar observations were reported in [51, 57] in which the HAZ bands appeared at temperatures just below the β -transus temperature in WAAM Ti-6Al-4V alloy. Similarly, in this study, the band formation temperature was slightly below the γ -transus temperature. Also, the FGF grains can be locally refined, even when reheated slightly below the γ -transus. The grain coarsening was not noticeably observed in this study, and the HAZ bands were mostly comprised of coarse grains. The formation of HAZ bands can only occur when subsequent layers reheat the CG-HAZ of the previous layer to a temperature above AC1, but not enough to austenitize it. Although the HAZ bands exhibit uneven and slightly coarser grains, similar to the undesirable inter-critical HAZ, they differ in being fully ferritic HAZ bands devoid of brittle phases like martensite and martensiteaustenite constituents [58, 59]. In the PGAM-AM section, it was sometimes challenging to distinguish the width of the CG-HAZ affected by inter-critical annealing from the subsequent layer. As illustrated in Figure 8(A), these HAZ bands can be difficult to eliminate and can persist even after subsequent heat treatments well below the normalizing temperature. However, the mechanical properties, mainly tensile strength, were minimally affected, as shown in Figure 10.

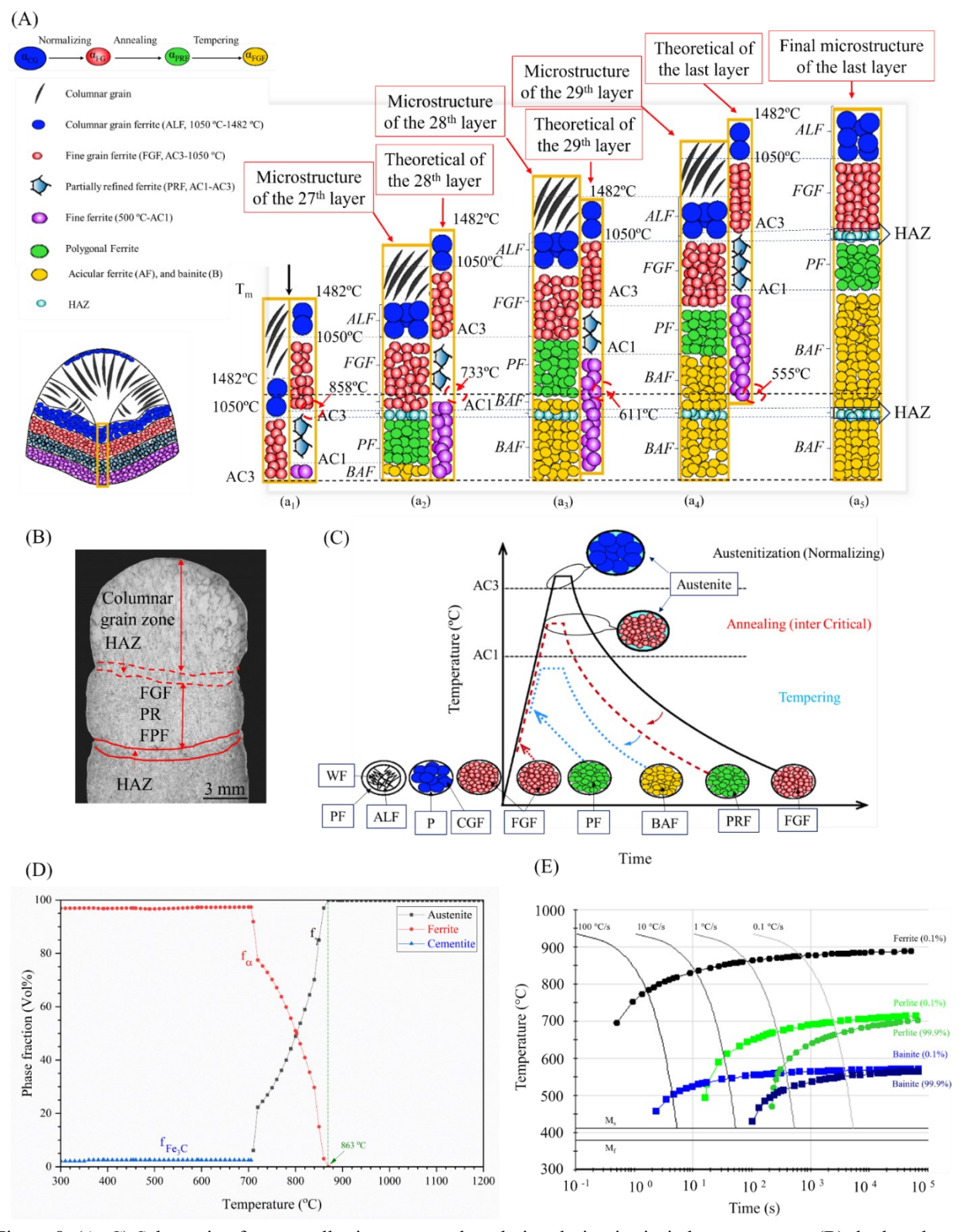


Figure 8. (A, C) Schematic of an overall microstructural evolution during intrinsic heat treatment, (B) the last three deposited layers with a consistent interlayer temperature of ~100 °C. (D) Equilibrium phase fraction variation for ferrite and austenite against calculated using JMatPro. (E) Continuous Cooling Transformation (CCT) diagram generated by exporting data from the JMatPro software for the specified composition.

3.2. Mechanical properties

3.2.1. Vickers microhardness Measurement

Figure 9(A) illustrates the variation in the Vickers microhardness values of the thin wall deposited layers. Regardless of the applied pulse frequency, the microhardness was slightly higher at the bottom and top layers. In the initial layers, typically up to 2 mm, the fast-cooling rate induced by the rigid and cool substrate, with its faster heat dissipation capability, resulted in the formation of fine-grained structures in the deposited materials. Moreover, the materials deposited on the top layer did not undergo thermal cycling and hence also maintained fine-grained structures. The highest Vickers microhardness values were associated with the acicular ferrite and bainite regions at the bottom and top layers, with values of about 240-260 HV_{0.2}. The Vickers microhardness values in the middle region were about 220-230 HV_{0.2}. The reduction in microhardness values was related to the formation of polygonal ferrite grain with the trace amount of pearlite due to the induced thermal cycles. It was apparent that the PGMA-AM processed low-alloy steels manufactured using pulse frequencies of 100-150 Hz have more uniform hardness. Exemplary indented areas on the manufactured part using a pulse frequency of 100 Hz are shown in Figure 9(B).

3.2.2. Tensile strength

Figure 10 shows the engineering stress-strain curves of the deposited low-alloy steel in the horizontal and vertical directions, and values are summarized in Table3. Although the attained average values of tensile test results were roughly the same in both directions, different samples showed different yield and tensile strength values. This suggests that there was no major anisotropy in the tensile strength of the PGMA-AM processed low-alloy steel, which was attributed to the similar microstructure in the vertical and horizontal direction in each deposited specimen. Recent studies have also reported an isotropic tensile strength for WAAM-processed low-alloy steel parts [34, 60]. Amongst tested specimens, the deposited part with a pulse frequency of 100 Hz showed the highest tensile strength and elongation values. The uniformity of the tensile strength in the longitudinal and vertical directions is more related to the uniformity and homogeneity of the microstructure. This isotropy in the mechanical behavior of each deposited wall was thought to be associated with the preparation of tensile specimens from the middle area (2<X<Y-2 mm) of each wall, in which the microstructure was mainly composed of ferritic grains. However, the ferritic grain size varied from sample to sample deposited using different pulse frequencies, thus, varied

tensile behavior was observed. The pulse frequency could affect the phase transformation rate and cooling condition, which directly affected transient layers in deposited materials.

The relationship between grain size and material strength can be described mathematically using the well-established Hall-Petch equation, as depicted below:

$$\sigma_{v} = \sigma_0 + kd^{-\frac{1}{2}} \tag{1}$$

In this equation, σ_v represents the material yield strength, while d signifies the average grain diameter. Additionally, σ_0 and K stand as material constants, with σ_0 representing the lattice's resistance to dislocation motion, and K serving as the strengthening coefficient [61]. Increasing frequencies from 50 Hz to 100 Hz leads to a finer grain structure in the material. Smaller grain sizes generally result in increased strength and hardness due to the grain boundaries acting as barriers to dislocation movement. The 100 Hz frequency caused a more uniform and consistent deposition of material and reduced the presence of defects and inconsistencies. The decrease in UTS value observed at frequency 150 Hz, rather than 100 Hz, can be described to the rise in temperatures within the interpass regions. This temperature elevation places these regions within the stability zone of the ferrite + austenite phase, which occurs between the AC₁ and AC₃ temperatures. Consequently, this leads to the formation of a specific region referred to as the intercritical heat-affected zone (ICHAZ) adjacent to each melting pool created in the previously deposited pass [62, 63]. In this area, there is possibility for the nucleation of the austenite phase along the boundaries of bainite laths or the prior austenite grain boundaries. This nucleation occurs due to the relatively high solid solubility of carbon in the austenite phase. Subsequently, as carbon atoms continue to diffuse from the matrix (comprising Ferrite + Bainite) into the nucleated austenite phase, the austenite phase experiences slight growth. This phenomenon takes place despite the low carbon concentration of the ER70S-6 wire. When this region experiences rapid cooling, if the carbon content is low, or if there are not enough alloying elements present to stabilize the austenite at room temperature (ER70S-6), the reverted austenite phase undergoes a transformation into the martensite-austenite (MA) constituent. This transformation results in the formation of localized brittle zones within the (ICHAZ) [64-66]. Furthermore, even though the grain size remains consistent, both the yield strength (YS) and ultimate tensile strength (UTS) values at a frequency of 100 Hz are ~50 MPa greater than those observed at 150 Hz.

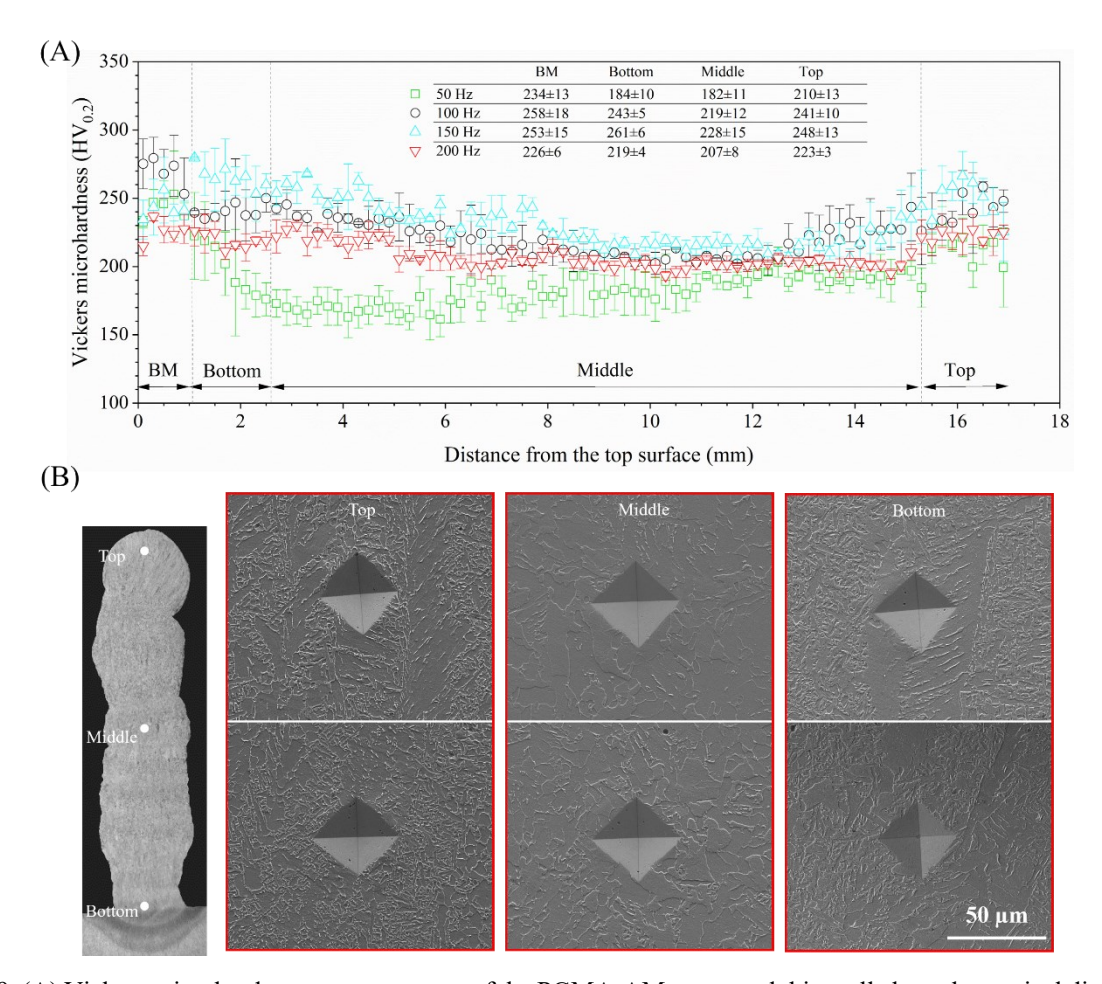


Figure 9. (A) Vickers microhardness measurements of the PGMA-AM processed thin wall along the vertical direction. (B) Exemplary indented regions on the manufactured part using a pulse frequency of 100 Hz.

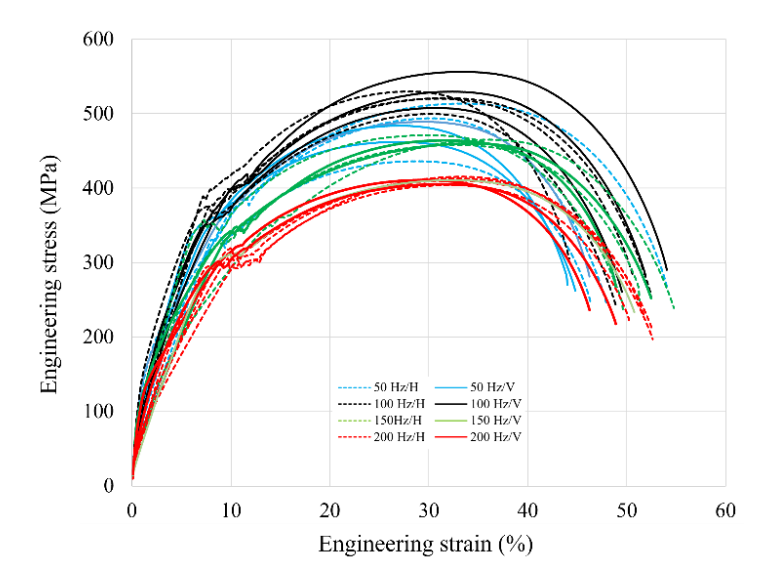


Figure 10. The engineering stress-strain curves for PGMA-AM specimens in both the horizontal and vertical directions.

Table3. Average values of yield strength (YS), ultimate tensile strength (UTS), and elongation (EL) results for samples tested in the horizontal and vertical directions.

AM processed parts	YS (MPa)	UTS (MPa)	EL (%)			
PGMA-AM - 50 Hz	Н	350±14	480±33	49.1±2.8	This study	
	V	351±7	477±11	44.9±0.8		
PGMA-AM - 100 Hz	Н	377±8	512±10	50.7±1.4		
	V	375±6	522±11	51.5±1.5		
PGMA-AM - 150 Hz	Н	338±13	462±6	51.6±1.8		
	V	347±4	460±3	50.7±1.7		
PGMA-AM - 200 Hz	Н	299±4	409±3	51.5±1.0]	
	V	304±8	408±3	48.5±1.7		
WAAM of ER-70S-6	Н	320±6	729±8		[17]	
	V	362±8	479±7			
	Н	258	475		[67]	
	V	266	478			
	Н	320	429			
	V	362	479			
	Н	396±26	503±21	35±2	[69]	
	V			12±3		
WAAM of ER-70S-6	380-480	480-520	13-28	[34]		
Wrought ASTM 36	250	400-550	20-23	[70]		
As-welded ER70S-6 with 100% CO	470	590	25	[71]		

3.2.3. Impact Test

The Charpy V-notch impact test results for both Horizontal and Vertical samples were conducted at five different temperatures: -150°C, -100°C, -50°C, 0°C, and 25°C (room temperature). The impact test results are presented in Figure 11, illustrating the curve fitting of all the samples, encompassing the entire structure, and reveals that the ductile to brittle transition temperature (DBTT) is approximately -50°C. The DBTT was determined by finding the temperature at which impact energy levels intersect between the upper and lower energy shelves. Furthermore, these findings demonstrate that the DBTT remains consistent and is not influenced by the orientation of the samples. Notably, the average absorbed energy values for the horizontal samples at all five temperatures surpass those of the vertical samples. This can be attributed to the horizontal samples having a uniform ferritic structure without defects. The development of uniform and smaller ferritic grains in the Horizontal samples contributes to increased yield strength and tensile strength, thereby enhancing ductile fracture mechanisms. In contrast, the vertical samples exhibit a periodic microstructure consisting of acicular ferrite and bainitic phases, which is expected to make them more brittle and prone to crack propagation [72]. Multipass weldments comprise HAZs, including coarse grain, fine grain, intercritically reheated coarse, and fine grain

HAZs. Due to the thin walls of the structure, the repeated thermal cycles continually reheat the same material in a vertical progression as the wall is constructed. In other words, each section in the middle of the building height generally undergoes similar thermal cycles, which can induce microstructural changes. This recurrent cyclical process results in a more uniform microstructure of polygonal ferrite. Consequently, this welding technique leads to a relatively low variability in toughness compared to literature [73-76].

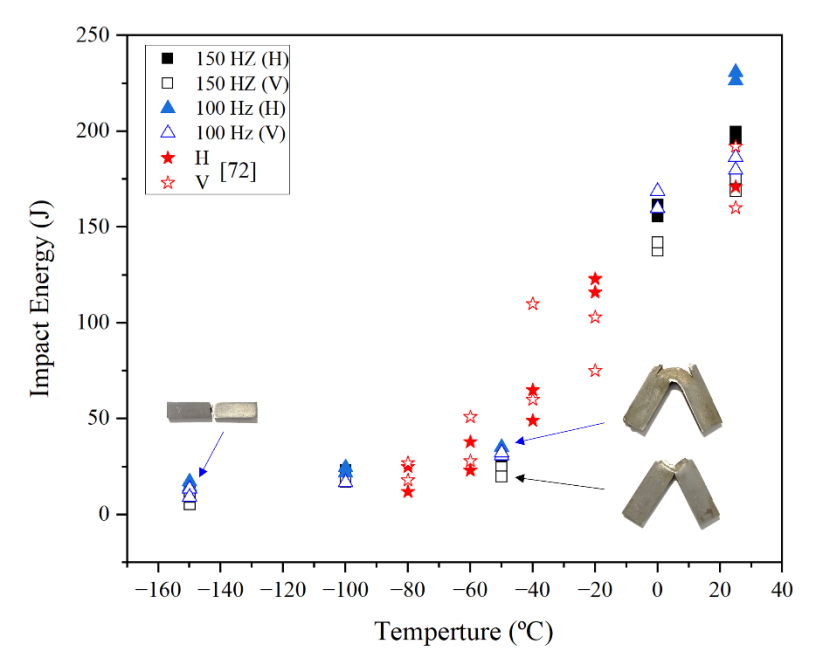


Figure 11. Charpy v-notch impact test results on selected samples.

3.2.4. Fractography

Figure 12 displays the fracture surfaces on both vertical and horizontal specimens. The horizontal samples exhibited various conical and cup-shaped dimples, consistent with [66], and showed no signs of discontinuities, such as the absence of a lack of fusion pores or cracks. This demonstrates that the fracture mechanism was mainly a ductile failure, with the fracture initiation controlled by the nucleation of microvoids in the identified strain region. Furthermore, merging microvoids generated cup and cone-shaped fracture surfaces [25]. In the case of the vertical samples, the degree of plastic deformation was less noticeable, and while dimples were present on the fracture surface, their morphology was slightly different. This phenomenon could be related to a shift in the failure mechanism during tensile testing of vertical samples. Due to the formation of river-like cleavage facets, as well as the lack of fusion and equiaxed dimples, the fracture

mechanism switched to a mixed mode of ductile and brittle fracture. The lower ductility of vertical samples could be attributed to this behavior.

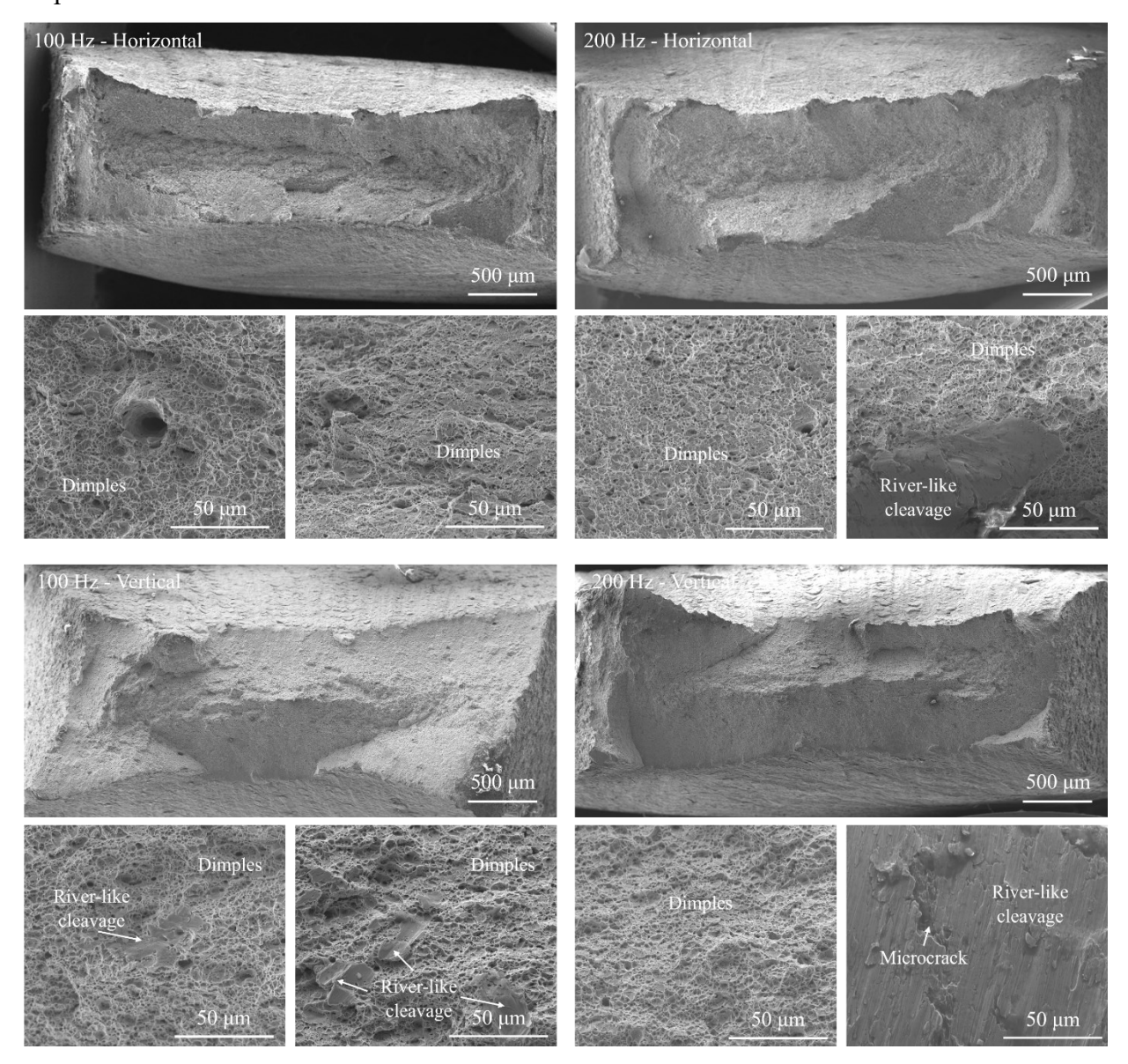


Figure 12. SEM micrographs from the fracture surface of PGMA-AM processed low-carbon low-alloy steel.

4. Conclusion

This study examined the effects of pulse frequency on the microstructure and mechanical properties of low-carbon low-alloy steel samples produced using wire arc additive manufacturing (WAAM). The following concluding remarks were achieved:

- 1. The process of PGMA-AM makes it possible to manufacture thin-walled low-carbon steel components with high density and minimal defects such as cracks and inadequate fusions between adjacent layers.
- 2. The results showed that increasing the pulse frequency potentially led to higher pulsed arc pressure, thus, a finer grain microstructure and better mechanical properties were achieved. The grain size decreased with increasing pulse frequency up to 150 Hz and then increased with higher pulse frequencies due to the fluctuation of the weld puddle. The optimum grain refinement was achieved at frequencies between 100 and 150 Hz.
- 3. The microstructure of the deposited wall had three distinct regions, with a wide middle region consisting of fine polygonal ferrite and pearlite phases. The bottom layer was made up of acicular ferrite and bainite, while the top region was confined. Vickers microhardness measurements showed the decency of microstructure with grain size and morphology of the present phases at different regions.
- 4. The average toughness of the horizontal samples at various temperatures exhibited similarity and exceeded that of the vertical samples. This difference in impact energy can be attributed to the microstructural distinctions between the two sets of samples.
- 5. The tensile strength of the deposited part was homogeneous in both the vertical and horizontal directions, in which the highest yield strength, tensile strength, and ductility of 377 PMA, 522 MPA, and 52%, respectively, were achieved for the deposited alloy with a pulse frequency of 100 Hz. The morphology of the fracture surface had the characteristic dimple form, with more significant and profound dimples observed in the horizontal samples, indicating greater ductility along that direction.

Acknowledgement

Financial support for this research at the University of Windsor was provided by the Natural Sciences and Engineering Research Council of Canada (NSERC). AM would like to acknowledge the startup funding from the Department of Mechanical, Materials and Aerospace Engineering and Armour College of Engineering at Illinois Institute of Technology at Chicago, Illinois. AM and ID acknowledge partial support from the National Science Foundation under grant number DMR-2050916.

Reference

- [1] Q. Wang *et al.*, "Microstructure evolution and EBSD analysis of a graded steel fabricated by laser additive manufacturing," *Vacuum*, vol. 141, pp. 68-81, 2017.
- [2] X. Xu, J. Ding, S. Ganguly, C. Diao, and S. Williams, "Preliminary investigation of building strategies of maraging steel bulk material using wire+ arc additive manufacture," *Journal of Materials Engineering and Performance*, vol. 28, no. 2, pp. 594-600, 2019.
- [3] M. Ghaffari, A. V. Nemani, M. Rafieazad, and A. Nasiri, "Effect of solidification defects and HAZ softening on the anisotropic mechanical properties of a wire arc additive-manufactured low-carbon low-alloy steel part," *Jom*, vol. 71, no. 11, pp. 4215-4224, 2019.
- [4] Y. Wang, X. Chen, and S. Konovalov, "Additive manufacturing based on welding arc: a low-cost method," *Journal of Surface Investigation: X-Ray, Synchrotron and Neutron Techniques,* vol. 11, no. 6, pp. 1317-1328, 2017.
- [5] J. Xiong, Y. Li, R. Li, and Z. Yin, "Influences of process parameters on surface roughness of multi-layer single-pass thin-walled parts in GMAW-based additive manufacturing," *Journal of Materials Processing Technology*, vol. 252, pp. 128-136, 2018.
- [6] D. Yang, G. Wang, and G. Zhang, "A comparative study of GMAW-and DE-GMAW-based additive manufacturing techniques: thermal behavior of the deposition process for thin-walled parts," *The International Journal of Advanced Manufacturing Technology,* vol. 91, no. 5-8, pp. 2175-2184, 2017.
- [7] W. Yangfan, C. Xizhang, and S. Chuanchu, "Microstructure and mechanical properties of Inconel 625 fabricated by wire-arc additive manufacturing," *Surface and Coatings Technology*, vol. 374, pp. 116-123, 2019.
- [8] K. Hoefer, A. Haelsig, and P. Mayr, "Arc-based additive manufacturing of steel components—comparison of wire-and powder-based variants," *Welding in the World,* vol. 62, no. 2, pp. 243-247, 2018.
- [9] X. Chen, J. Li, X. Cheng, B. He, H. Wang, and Z. Huang, "Microstructure and mechanical properties of the austenitic stainless steel 316L fabricated by gas metal arc additive manufacturing," *Materials Science and Engineering: A*, vol. 703, pp. 567-577, 2017.
- [10] A. Mostafaei *et al.*, "Defects and anomalies in powder bed fusion metal additive manufacturing," *Current Opinion in Solid State and Materials Science*, vol. 26, no. 2, p. 100974, 2022.
- [11] Y. Luo, J. Li, J. Xu, L. Zhu, J. Han, and C. Zhang, "Influence of pulsed arc on the metal droplet deposited by projected transfer mode in wire-arc additive manufacturing," *Journal of Materials Processing Technology*, vol. 259, pp. 353-360, 2018.
- [12] W. E. Frazier, "Metal additive manufacturing: a review," *Journal of Materials Engineering and Performance*, vol. 23, no. 6, pp. 1917-1928, 2014.
- [13] Y. Li, Y. Sun, Q. Han, G. Zhang, and I. Horváth, "Enhanced beads overlapping model for wire and arc additive manufacturing of multi-layer multi-bead metallic parts," *Journal of Materials Processing Technology*, vol. 252, pp. 838-848, 2018.
- [14] J. Xiong, Z. Yin, and W. Zhang, "Forming appearance control of arc striking and extinguishing area in multi-layer single-pass GMAW-based additive manufacturing," *The International Journal of Advanced Manufacturing Technology*, vol. 87, no. 1-4, pp. 579-586, 2016.
- [15] J. Xiong, G. Zhang, and W. Zhang, "Forming appearance analysis in multi-layer single-pass GMAW-based additive manufacturing," *The International Journal of Advanced Manufacturing Technology*, vol. 80, no. 9-12, pp. 1767-1776, 2015.
- [16] X. Zhang *et al.*, "Study on microstructure and tensile properties of high nitrogen Cr-Mn steel processed by CMT wire and arc additive manufacturing," *Materials & Design*, vol. 166, p. 107611, 2019.

- [17] V. T. Le and H. Paris, "On the use of gas-metal-arc-welding additive manufacturing for repurposing of low-carbon steel components: microstructures and mechanical properties," *Welding in the World*, vol. 65, no. 1, pp. 157-166, 2021.
- [18] D. Ding, Z. Pan, D. Cuiuri, H. Li, S. van Duin, and N. Larkin, "Bead modelling and implementation of adaptive MAT path in wire and arc additive manufacturing," *Robotics and Computer-Integrated Manufacturing*, vol. 39, pp. 32-42, 2016.
- [19] Y. Li, Q. Han, G. Zhang, and I. Horváth, "A layers-overlapping strategy for robotic wire and arc additive manufacturing of multi-layer multi-bead components with homogeneous layers," *The International Journal of Advanced Manufacturing Technology,* vol. 96, no. 9-12, pp. 3331-3344, 2018.
- [20] F. Youheng, W. Guilan, Z. Haiou, and L. Liye, "Optimization of surface appearance for wire and arc additive manufacturing of Bainite steel," *The International Journal of Advanced Manufacturing Technology*, vol. 91, no. 1-4, pp. 301-313, 2017.
- [21] M. Rafieazad, A. V. Nemani, M. Ghaffari, and A. Nasiri, "On microstructure and mechanical properties of a low-carbon low-alloy steel block fabricated by wire arc additive manufacturing," *Journal of Materials Engineering and Performance*, vol. 30, pp. 4937-4945, 2021.
- [22] C. Haden, G. Zeng, F. Carter III, C. Ruhl, B. Krick, and D. Harlow, "Wire and arc additive manufactured steel: Tensile and wear properties," *Additive Manufacturing*, vol. 16, pp. 115-123, 2017.
- [23] K. Liu, D. Wang, C. Deng, B. Gong, and S. Wu, "Improved microstructure heterogeneity and low-temperature fracture toughness of C–Mn weld metal through post weld heat treatment," *Materials Science and Engineering: A*, vol. 770, p. 138541, 2020.
- [24] Q. Wu *et al.*, "Obtaining uniform deposition with variable wire feeding direction during wire-feed additive manufacturing," *Materials and Manufacturing Processes*, vol. 32, no. 16, pp. 1881-1886, 2017.
- [25] X. Xu, S. Ganguly, J. Ding, S. Guo, S. Williams, and F. Martina, "Microstructural evolution and mechanical properties of maraging steel produced by wire+ arc additive manufacture process," *Materials Characterization*, vol. 143, pp. 152-162, 2018.
- [26] S. Ríos, P. A. Colegrove, and S. W. Williams, "Metal transfer modes in plasma Wire+ Arc additive manufacture," *Journal of Materials Processing Technology*, vol. 264, pp. 45-54, 2019.
- [27] R. Hu, X. Chen, G. Yang, S. Gong, and S. Pang, "Metal transfer in wire feeding-based electron beam 3D printing: Modes, dynamics, and transition criterion," *International Journal of Heat and Mass Transfer*, vol. 126, pp. 877-887, 2018.
- [28] A. Vahedi Nemani, M. Ghaffari, and A. Nasiri, "On the post-printing heat treatment of a wire arc additively manufactured ER70S part," *Materials*, vol. 13, no. 12, p. 2795, 2020.
- [29] K. Pal and S. K. Pal, "Effect of pulse parameters on weld quality in pulsed gas metal arc welding: a review," *Journal of materials engineering and performance*, vol. 20, no. 6, pp. 918-931, 2011.
- [30] Q. Wu, Z. Ma, G. Chen, C. Liu, D. Ma, and S. Ma, "Obtaining fine microstructure and unsupported overhangs by low heat input pulse arc additive manufacturing," *Journal of Manufacturing Processes*, vol. 27, pp. 198-206, 2017.
- [31] J. Lin *et al.*, "Microstructural evolution and mechanical properties of Ti-6Al-4V wall deposited by pulsed plasma arc additive manufacturing," *Materials & Design*, vol. 102, pp. 30-40, 2016.
- [32] G. Chen, Z. Ma, and C. Liu, "Investigation of the benefits of pulse current for the additive manufacture of Ti-6Al-4V," in *2016 5th International Conference on Environment, Materials, Chemistry and Power Electronics*, 2016: Atlantis Press.
- [33] F. Wang, S. Williams, and M. Rush, "Morphology investigation on direct current pulsed gas tungsten arc welded additive layer manufactured Ti6Al4V alloy," *The international journal of advanced manufacturing technology*, vol. 57, no. 5-8, pp. 597-603, 2011.

- [34] N. Sridharan, M. W. Noakes, A. Nycz, L. J. Love, R. R. Dehoff, and S. S. Babu, "On the toughness scatter in low alloy C-Mn steel samples fabricated using wire arc additive manufacturing," *Materials Science and Engineering: A*, vol. 713, pp. 18-27, 2018.
- [35] S. Babu and H. Bhadeshia, "Transition from bainite to acicular ferrite in reheated Fe–Cr–C weld deposits," *Materials Science and Technology*, vol. 6, no. 10, pp. 1005-1020, 1990.
- Y. Chen *et al.*, "Dendritic microstructure and hot cracking of laser additive manufactured Inconel 718 under improved base cooling," *Journal of Alloys and Compounds*, vol. 670, pp. 312-321, 2016.
- [37] M. Liberini *et al.*, "Selection of optimal process parameters for wire arc additive manufacturing," *Procedia Cirp*, vol. 62, pp. 470-474, 2017.
- [38] V. Subravel, G. Padmanaban, and V. Balasubramanian, "Effect of pulse frequency on tensile properties and microstructural characteristics of gas tungsten arc welded AZ31B magnesium alloy," *Transactions of the Indian Institute of Metals*, vol. 68, no. 3, pp. 353-362, 2015.
- [39] F. Wang, S. Williams, and M. Rush, "Morphology investigation on direct current pulsed gas tungsten arc welded additive layer manufactured Ti6Al4V alloy," *The international journal of advanced manufacturing technology,* vol. 57, no. 5, pp. 597-603, 2011.
- [40] S. Kou, "Welding metallurgy," *New Jersey, USA,* pp. 431-446, 2003.
- [41] Y. Sharir, J. Pelleg, and A. Grill, "Effect of arc vibration and current pulses on microstructure and mechanical properties of TIG tantalum welds," *Metals Technology*, vol. 5, no. 1, pp. 190-196, 1978.
- [42] A. ASTM, "1033-04," Standard Practice for Quantitative Measurement and Reporting of Hypoeutectoid Carbon and Low-Alloy Steel Phase Transformations, pp. 1-14, 2004.
- [43] K. Andrews, "Empirical formulae for the calculation of some transformation temperatures," *J. Iron Steel Inst.*, pp. 721-727, 1965.
- [44] R. W. K. Honeycombe, "Steels microstructure and properties," *Metallurgy and materials science*, vol. 1, 1995.
- [45] Y. Li, S. Wu, H. Li, Y. Dong, and F. Cheng, "Submerged arc additive manufacturing (SAAM) of low-carbon steel: Effect of in-situ intrinsic heat treatment (IHT) on microstructure and mechanical properties," *Additive Manufacturing*, vol. 46, p. 102124, 2021.
- [46] S. Yaowu, "Material welding engineering," in *China Materials Engineering Canon*: Chemical Industry Press Beijing, 2005.
- [47] M. Ghaffari, A. Vahedi Nemani, M. Rafieazad, and A. Nasiri, "Effect of solidification defects and HAZ softening on the anisotropic mechanical properties of a wire arc additive-manufactured low-carbon low-alloy steel part," *Jom*, vol. 71, pp. 4215-4224, 2019.
- [48] G. Xian *et al.*, "Effect of heat input on microstructure and mechanical property of wire-arc additive manufactured Ti-6Al-4V alloy," *Welding in the World*, vol. 66, no. 5, pp. 847-861, 2022.
- [49] T. A. Rodrigues, V. Duarte, J. A. Avila, T. G. Santos, R. Miranda, and J. Oliveira, "Wire and arc additive manufacturing of HSLA steel: Effect of thermal cycles on microstructure and mechanical properties," *Additive Manufacturing*, vol. 27, pp. 440-450, 2019.
- [50] M. Graf, A. Hälsig, K. Höfer, B. Awiszus, and P. Mayr, "Thermo-mechanical modelling of wire-arc additive manufacturing (WAAM) of semi-finished products," *Metals*, vol. 8, no. 12, p. 1009, 2018.
- [51] A. Ho, H. Zhao, J. W. Fellowes, F. Martina, A. E. Davis, and P. B. Prangnell, "On the origin of microstructural banding in Ti-6Al4V wire-arc based high deposition rate additive manufacturing," *Acta Materialia*, vol. 166, pp. 306-323, 2019.
- [52] J.-S. Wang, C.-C. Hsieh, C.-M. Lin, E.-C. Chen, C.-W. Kuo, and W. Wu, "The effect of residual stress relaxation by the vibratory stress relief technique on the textures of grains in AA 6061 aluminum alloy," *Materials Science and Engineering: A*, vol. 605, pp. 98-107, 2014.
- [53] O. Panchenko, I. Kladov, D. Kurushkin, L. Zhabrev, E. Ryl'kov, and M. Zamozdra, "Effect of thermal history on microstructure evolution and mechanical properties in wire arc additive manufacturing

- of HSLA steel functionally graded components," *Materials Science and Engineering: A,* vol. 851, p. 143569, 2022.
- [54] W. Hackenhaar, J. A. Mazzaferro, C. C. Mazzaferro, N. Grossi, and G. Campatelli, "Effects of different WAAM current deposition modes on the mechanical properties of AISI H13 tool steel," *Welding in the World,* vol. 66, no. 11, pp. 2259-2269, 2022.
- [55] S. Kou, "Welding metallurgy," New Jersey, USA, vol. 431, no. 446, pp. 223-225, 2003.
- [56] A. Caballero, J. Ding, S. Ganguly, and S. Williams, "Wire+ Arc Additive Manufacture of 17-4 PH stainless steel: Effect of different processing conditions on microstructure, hardness, and tensile strength," *Journal of Materials Processing Technology*, vol. 268, pp. 54-62, 2019.
- [57] M. Bermingham, D. StJohn, J. Krynen, S. Tedman-Jones, and M. Dargusch, "Promoting the columnar to equiaxed transition and grain refinement of titanium alloys during additive manufacturing," *Acta Materialia*, vol. 168, pp. 261-274, 2019.
- [58] N. Huda, Y. Wang, L. Li, and A. P. Gerlich, "Effect of martensite-austenite (MA) distribution on mechanical properties of inter-critical Reheated Coarse Grain heat affected zone in X80 linepipe steel," *Materials Science and Engineering: A,* vol. 765, p. 138301, 2019.
- [59] P. Karimi *et al.*, "Columnar-to-equiaxed grain transition in powder bed fusion via mimicking casting solidification and promoting in situ recrystallization," *Additive Manufacturing*, vol. 46, p. 102086, 2021.
- [60] C. Haden, G. Zeng, F. Carter, C. Ruhl, B. Krick, and D. Harlow, "Wire and arc additive manufactured steel: tensile and wear properties. Addit. Manuf. 16, 115–123 (2017)," ed.
- [61] E. Hall, "The deformation and ageing of mild steel: III discussion of results," *Proceedings of the Physical Society. Section B,* vol. 64, no. 9, p. 747, 1951.
- [62] B. Kim, S. Lee, N. Kim, and D. Lee, "Microstructure and local brittle zone phenomena in high-strength low-alloy steel welds," *Metallurgical Transactions A*, vol. 22, pp. 139-149, 1991.
- [63] O. Akselsen, Ø. Grong, and J. Solberg, "Structure–property relationships in intercritical heat affected zone of low-carbon microalloyed steels," *Materials science and technology,* vol. 3, no. 8, pp. 649-655, 1987.
- [64] Y. Li and T. Baker, "Effect of morphology of martensite—austenite phase on fracture of weld heat affected zone in vanadium and niobium microalloyed steels," *Materials science and technology*, vol. 26, no. 9, pp. 1029-1040, 2010.
- [65] N. Huda, A. R. Midawi, J. Gianetto, R. Lazor, and A. P. Gerlich, "Influence of martensite-austenite (MA) on impact toughness of X80 line pipe steels," *Materials Science and Engineering: A,* vol. 662, pp. 481-491, 2016.
- [66] X. Shi *et al.*, "Selective laser melting-wire arc additive manufacturing hybrid fabrication of Ti-6Al-4V alloy: Microstructure and mechanical properties," *Materials Science and Engineering: A,* vol. 684, pp. 196-204, 2017.
- [67] J.-B. Yan, J. R. Liew, M.-H. Zhang, and J.-Y. Wang, "Mechanical properties of normal strength mild steel and high strength steel S690 in low temperature relevant to Arctic environment," *Materials & Design*, vol. 61, pp. 150-159, 2014.
- [68] V. T. Le, D. S. Mai, and Q. H. Hoang, "A study on wire and arc additive manufacturing of low-carbon steel components: process stability, microstructural and mechanical properties," *Journal of the Brazilian Society of Mechanical Sciences and Engineering*, vol. 42, pp. 1-11, 2020.
- [69] M. Rafieazad, M. Ghaffari, A. Vahedi Nemani, and A. Nasiri, "Microstructural evolution and mechanical properties of a low-carbon low-alloy steel produced by wire arc additive manufacturing," *The International Journal of Advanced Manufacturing Technology,* vol. 105, pp. 2121-2134, 2019.
- [70] A. International, "ASTM A36/A36M-19 Standard Specification for Carbon Structural Steel," ed: American Society for Testing and Materials International West Conshohocken ..., 2019.

- [71] "The Lincoln Electric Company: MIG (GMAW) WIRE n.d. SUPERARC G4Si1," ed https://lincolnelectric.com/assets/global/Products/ConsumableMIGGMAWWires-SuperArc-SuperArcG4Si1/c41025.pdf, 3 Sept 2020, pp. Mild Steel, Copper Coated, AWS ER70S-6.
- [72] B. Shassere, A. Nycz, M. W. Noakes, C. Masuo, and N. Sridharan, "Correlation of microstructure and mechanical properties of metal big area additive manufacturing," *Applied Sciences*, vol. 9, no. 4, p. 787, 2019.
- [73] M. A. Quintana, S. Babu, J. Major, C. Dallam, and M. James, "Weld Metal Toughness: Sources of Variation," in *International Pipeline Conference*, 2010, vol. 44212, pp. 599-608.
- [74] H. Song, G. Evans, and S. Babu, "Effect of microstructural heterogeneities on scatter of toughness in multi-pass weld metal of C–Mn steels," *Science and Technology of Welding and Joining,* vol. 19, no. 5, pp. 376-384, 2014.
- [75] A. Waqas, X. Qin, J. Xiong, C. Zheng, and H. Wang, "Analysis of ductile fracture obtained by charpy impact test of a steel structure created by robot-assisted GMAW-based additive manufacturing," *Metals*, vol. 9, no. 11, p. 1208, 2019.
- [76] Y. Zhao *et al.*, "Effects of microstructure on crack resistance and low-temperature toughness of ultra-low carbon high strength steel," *International Journal of Plasticity*, vol. 116, pp. 203-215, 2019.